Vibration Analysis of Pre-Twisted Blades with Symmetric and Asymmetric Airfoils Using the Ritz Method

Saeed Shokrollahi*, Alireza Norouzi, Salman Shafaghat,

Aerospace complex, Malek-Ashtar University of Technology, Tehran, Iran

Abstract: This study performs vibration analysis of pre-twisted rectangular and airfoil-section blades using a Ritz-based continuous classical beam–shaft reduced-order model (ROM), demonstrating its applicability in gas turbine design workflows. The framework incorporates pre-twist effects and static imbalance (CG–EA offset), which is horizontal in symmetric airfoils and also vertical in cambered or asymmetric airfoils. Discretization of the energy equations using trial functions yields the global mass and stiffness matrices, facilitating the vibration analysis of blades with complex geometries through a standard eigenvalue formulation. Validation is performed against finite element method (FEM) analyses using MSC Nastran and results from an advanced finite difference method (FDM) reported in the literature. The results show strong agreement while maintaining computational efficiency. The proposed framework provides a basis for ROM-based tools capable of performing computationally efficient aeroelastic analyses of continuous blade models, blade rows, and integrated gas turbines. Torsional, flapwise, and chordwise bending modes—including their couplings induced by pre-twist and static imbalances—are examined, and natural frequency trends for different imbalance configurations are presented as functions of pre-twist angle.

K E Y W O R D S

Free Vibration, Blade, Pre-twist, Ritz method

Nomenclature

xx: Fixed horizontal axis passing through the cross-section shear center

x: Coordinate along the xx axis

x_1x_1: Fixed horizontal axis passing through the cross-section centroid

I_{xx}: Second moment of area about the x_1x_1 axis

x_1: Coordinate along the x_1x_1 axis

α: Pre-twist angle

XX: Rotated x_1x_1 axis by the pre-twist angle

I_{XX}: Second moment of area about the XX axis

yy: Fixed vertical axis through cross-section shear center

y: Coordinate along the yy axis

y_1y_1: Fixed vertical axis through cross-section centroid

I_{yy}: Second moment of area about the $y_1y_1$axis

* Corresponding Author: Saeed Shokrollahi, Email: s_shokrollahi@mut.ac.ir, s_shokrollahi@yahoo.com

y_1: Coordinate along the y_1y_1 axis

YY: Rotated $y_1y_1$axis by pre-twist angle

I_{YY}: Second moment of area about the YY axis

I_{xy}: Product moment of area about the x_1x_1 and y_1y_1 axes

zz: Longitudinal axis

z: Spanwise coordinate

CG: Center of gravity

EA: Elastic axis

r_x: Projection of the CG-EA offset on x-axis

r_y: Projection of the CG-EA offset on y-axis

r_X: Projection of the CG-EA offset on X-axis

r_Y: Projection of the CG-EA offset on Y-axis

E: Young's modulus

G: Shear modulus

b: Cross-sectional width (chordwise direction)

d: Cross-sectional depth (thickness or flapwise direction)

l: Blade length

ρ: Density

A: Cross-sectional area

T: Kinetic energy

π: Strain energy

J: Torsional constant

C: Torsional rigidity

$I_{c.g.}$: Mass moment of inertia about the center of gravity

$I_{c.f.}$: Mass moment of inertia about the elastic axis

n: Number of modes

$x(z,t)$: In-Plane (chordwise/edgewise) bending displacement

$y(z,t)$: Out-of-plane (flapwise) bending displacement

$\theta(z,t)$: Torsional deformation

$T_{b,x}(\mathrm{t})$: Modal(generalized) coordinate for chordwise bending

$T_{b,y}(\mathrm{t})$: Modal(generalized) coordinate for flapwise bending

$T_{\theta}(\mathrm{t})$: Modal(generalized) coordinate for torsion

i ,j: Mode indices

$X^{(i)}(z)$: i-th chordwise bending mode shape

$Y^{(i)}(z)$: i-th flapwise bending mode shape

$\Theta^{(i)}(z)$: i-th torsional mode shape

$\vec{\mathrm{T}}$: Generalized coordinate vector

ϕ_{x_j}: j-th chordwise bending trial function

ϕ_{y_j}: j-th flapwise bending trial function

ϕ_{θ_j}: j-th torsion trial function

$c_{b,x_j}^{(i)}$: j-th Ritz constant (eigenvector component) for the i-th chordwise mode

$c_{b,y_j}^{(i)}$: j-th Ritz constant (eigenvector component) for the i-th flapwise mode

$c_{\theta_j}^{(i)}$: j-th Ritz constant (eigenvector component) for the i-th torsional mode

$[m]$: Global mass matrix

$[k]$: Global stiffness matrix

$[k_y]$: Flapwise bending stiffness matrix

$[k_x]$: Chordwise bending stiffness matrix

$[k_\theta]$: Torsional stiffness matrix

$[k_{xy}]$, $[k_{yx}]$: Coupled flapwise-chordwise stiffness matrices

$[m_y]$: Flapwise bending mass matrix

$[m_x]$: Chordwise bending mass matrix

$[m_\theta]$: Torsional mass matrix

$[m_{y\theta}]$, $[m_{\theta y}]$: Coupled flapwise-torsional mass matrices

$[m_{x\theta}]$, $[m_{\theta x}]$: Coupled chordwise-torsional mass matrices

T^*_{max}, D: Reference kinetic energy

π_{max}, N: Maximum strain energy

R: Rayleigh's quotient

M: Bending moment

V: Shear force

λ : Eigenvalue

I_x: Area moment of inertia about the xx axis

I_y: Area moment of inertia about the yy axis

$\vec{F}_{3n\times1}$: External load vector

$\vec{q}_{3n\times1}$: Displacement vector

x_I: Dimensionless horizontal CG-EA offset

y_I: Dimensionless vertical CG-EA offset

ω: Circular natural frequency

1. Introduction

For gas turbines—particularly aero-engines, which exemplify advanced engineering at the forefront of technological innovation—a thorough understanding of their core design and analysis fundamentals remains essential. Over time, classical engineering science and technology domains have converged, producing inherently complex, multidisciplinary challenges. A prime example is turbomachinery aeroelasticity, which requires coupled analysis of blade-row behavior and full-system gas turbine dynamics, demanding rigorous consideration during design certification at leading aero-engine manufacturers.

The occurrence of high-cycle fatigue (HCF), flutter, buffet, resonant vibrations, and noise—combined with prohibitive testing costs and the risk of catastrophic failure—necessitates the development of rapid, high-fidelity computational tools based on reduced-order modeling (ROM). Such tools are essential during the conceptual and preliminary design phases to address vibration and aeroelastic challenges in gas turbines. These ROM frameworks must incorporate modal representations of blade dynamics that account for critical factors such as pre-twist and asymmetric airfoil cross-sections. Over recent decades, these capabilities have been realized through various modeling approaches and solution methods.

Static imbalance effects at different pre-twist angles were investigated experimentally by Carnegie [1], while Subrahmanyam and Kaza [2] studied the effects of different combinations of static imbalances in Carnegie's blade airfoils using the advanced finite difference method. The transformation method, as described by Carnegie [3], involves converting the original differential equations of motion into ten simultaneous first-order differential equations. These equations are subsequently solved via a finite-difference step-by-step procedure.

Maney investigators have studied the effect of pre-twist in blades. Modeling approaches are generally classified as either continuous or discrete. Reported solution methods include the Rayleigh method [1,4–7], Ritz method [8–12], Galerkin method [8,13,14], collocation method

[15], Reissner method [16,17], perturbation method [18,19], transformation method [3,4,20–23], station function method [24,25], lumped parameter method [26], Myklestad method [27], Holzer-Myklestad method [28], extended Holzer-Myklestad method [29], Stodola method [30], Adomian modified decomposition method (AMDM) [31], and the finite element method (FEM) [32–38]. However, the investigation of static imbalance effects at different pre-twist angles, as well as for different combinations of static imbalances in airfoils, has not been addressed using the Ritz method in the literature.

This study extends previous works by employing the Ritz method to model symmetrical and asymmetrical pre-twisted blade cross-sections, deriving their global mass and stiffness matrices as a foundation for reduced-order aeroelastic formulations. Natural frequency variations are analyzed with respect to pre-twist angles, highlighting the influence of static imbalance combinations. The proposed methodology is validated against numerical solutions from MSC Nastran and advanced finite-difference results from the literature [2]. The approach also shows potential for deriving reduced modal equations in ROM-based blade-row aeroelastic formulations [39,40].

2. Problem Statement

This study first reviews the modal behavior of pre-twisted rectangular-section blades using the Ritz method, and then investigates the modal characteristics of symmetric and asymmetric airfoil-section blades under pre-twist. Carnegie's blades [1–3,20], which include both rectangular and airfoil cross-sections and feature pre-twist angles ranging from 0° to 90° in 15° increments, serve as reference configurations, as shown in Fig. 1.

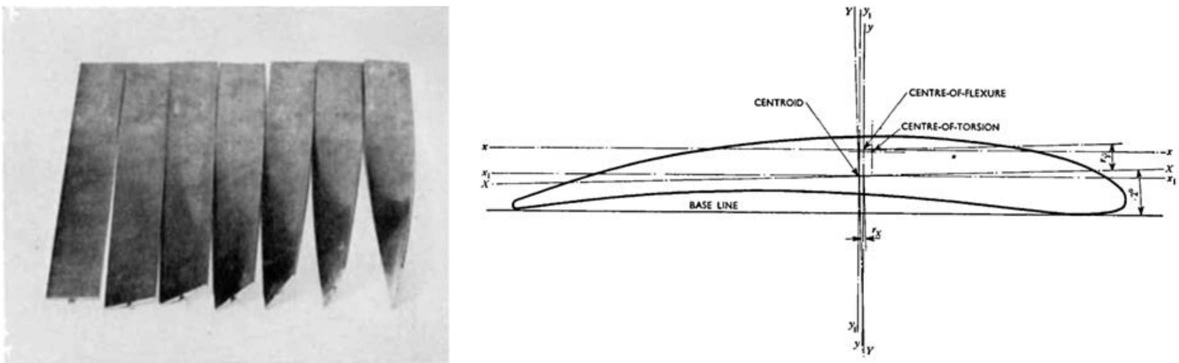

Fig. 1. Carnegie's pre-twisted blades used as reference configurations [1,41]

3. Blade Dynamics Modeling Approches as a Basis For Aeroelastic Analysis

Non-experimental structural dynamics analysis of blades and blade rows, as a basis for turbomachinery aeroelasticity, typically employs three solution approaches—analytical, approximate analytical, and numerical—alongside two modeling approaches: typical-section modeling and continuous modeling [42]. While typical-section modeling continues to play an important role in cascade aeroelasticity research [43] and in the development of novel concepts [44], approximate analytical continuous modeling in blade-row aeroelasticity offers a viable alternative that significantly improves accuracy while avoiding the high computational cost associated with numerical simulations [40]. The typical-section methodology analyzes a representative blade cross-section (conventionally located at 75%–80% span for aerodynamic criticality, as shown in Fig. 2) rather than solving the full-blade governing equations. By deriving the vibration governing equation for this aerodynamically dominant section, blade-row structural dynamics can be modeled at its most fundamental level (Fig. 3) as a two-dimensional cascade.

Continuous modeling utilizes beam, shaft, and plate idealizations based on the targeted model characteristics. Beam formulations capture both in-plane (chordwise or edgewise) and out-of-plane (flapwise) bending behaviors, which are critical for blade analysis. The Euler–Bernoulli beam theory—excluding rotational inertia and shear deformation—is adopted here, as the difference with the Timoshenko model is very small (up to a maximum of 2.5% for the blade used in this study, as stated in [3]). This model provides sufficient accuracy for slender blades with slenderness ratios greater than 10. The aspect ratio (span-to-chord ratio) and slenderness ratio (span-to-thickness ratio) are critical geometric parameters governing validity. The shaft model captures torsional deformation. Specifically, the beam-shaft formulation accounts for both in-plane and out-of-plane bending as well as torsional deformation. Plate models, which describe plate-type vibration modes, are rarely employed in this context, due to their complexity, particularly at next turbomachinery aeroelastic considerations. The Rayleigh–Ritz method (an extension of the Rayleigh method) approximates continuous systems with infinite degrees of freedom (DOFs) using a user-defined finite-DOF system. This approximate analytical approach extracts natural frequencies and mode shapes equal in number to the selected DOFs. Convergence to the exact solution improves as the number of DOFs increases.

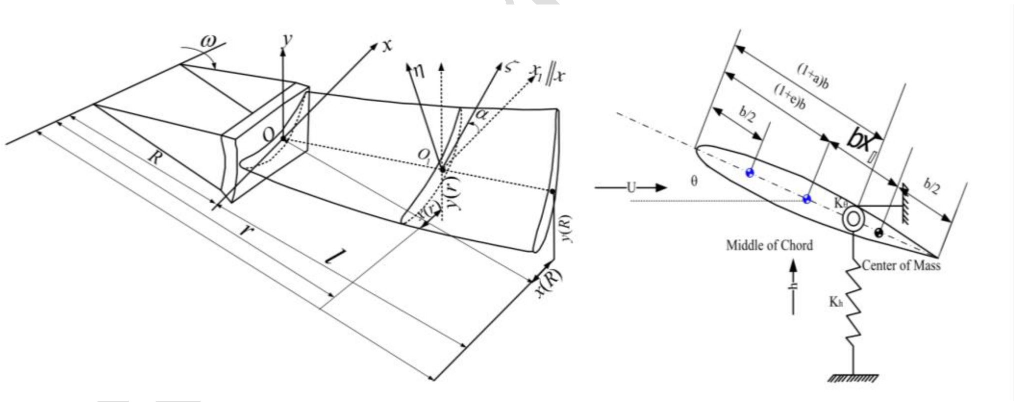

Fig. 2. Typical-section modeling of a blade [43]

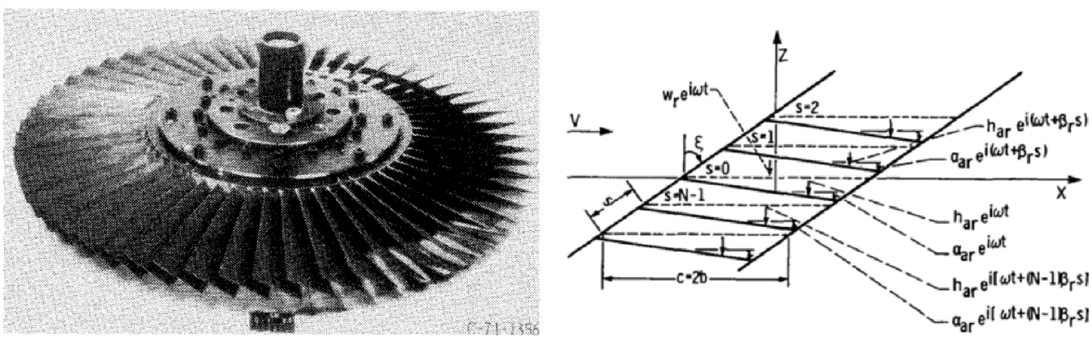

Fig. 3. Typical-section modeling of a blade row as a two-dimensional cascade [45]

4. Effects of Pre-Twist and Static Imbalances on Blade Modal Behaviour

Blade dynamics are Influenced by critical factors, including pre-twist and static imbalances. Figs. 4 and 5 show the vibration modes of two baseline cantilever blades (without pre-twist or static imbalances), which include flapwise bending, chordwise bending, torsion, longitudinal and plate-type modes.

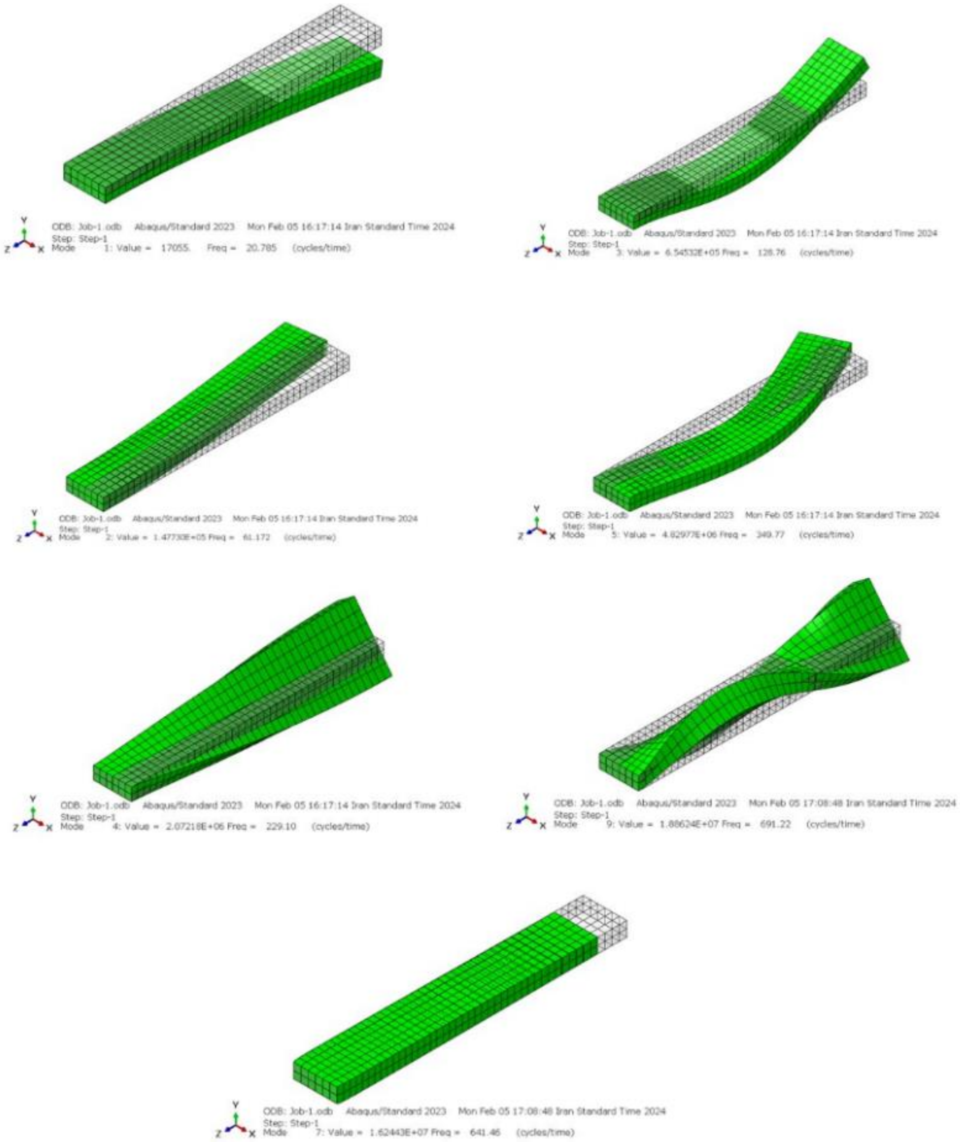

Fig. 4. Flapwise bending (1st row), chordwise bending (2nd row), torsional (3rd row), and longitudinal (4th row) mode shapes of a continuous cantilever model

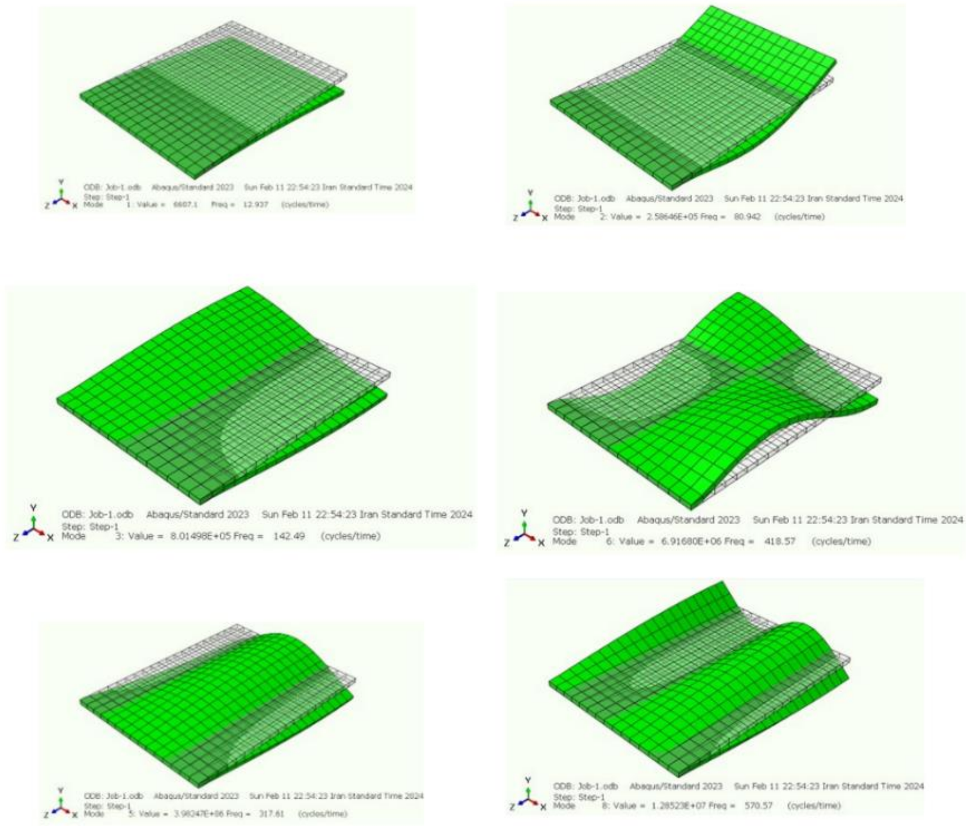

Fig. 5. Flapwise bending (1st row), torsional (2nd row), and plate-type (3rd row) mode shapes of a continuous cantilever model

The static imbalance parameter quantifies the dimensionless offset between the elastic axis (EA) and the center of gravity (CG), relative to the semi-chord (Fig. 6). This induces inertial coupling between torsional vibrations and both flapwise and chordwise bending vibrations through the off-diagonal terms of the mass matrix. Cross-sections symmetric about both axes (e.g., rectangular sections or doubly symmetric airfoils) exhibit zero static imbalance, while symmetric airfoils develop horizontal static imbalance, which introduces a coupled flapwise bending–torsion mode. Cambered or asymmetric airfoils develop vertical or both vertical and horizontal static imbalance, leading to coupled chordwise bending–torsion mode and coupled flapwise bending–torsion mode [1,46]. A coupled bending–torsion mode shape for a NACA 4415 airfoil-section model (Fig. 7) is illustrated in Fig. 8.

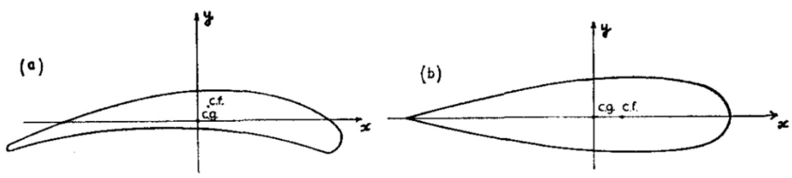

Fig. 6. Center of gravity (CG) and elastic axis (EA, or center of flexure, CF) for asymmetric (a) and symmetric (b) airfoils [3]

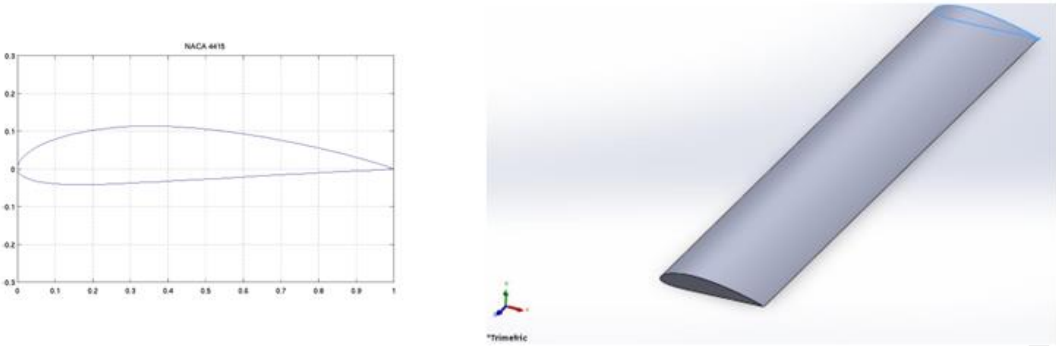

Fig. 7. NACA 4415 airfoil-section model

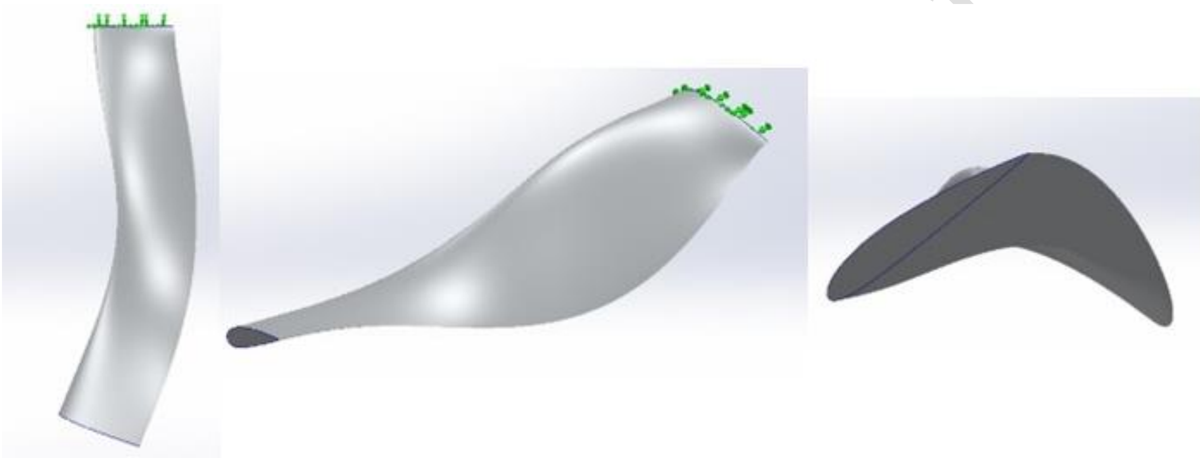

Fig. 8. Coupled bending–torsion mode shape for a NACA 4415 airfoil-section model

Pre-twist in gas turbine blades plays a crucial role. As linear rotational velocity increases with radial position from root to tip, the local flow velocity and aerodynamic forces intensify. Structurally, pre-twist optimizes spanwise aerodynamic load distribution to mitigate root torque accumulation, thereby preventing structural failure. Aerodynamically, it adjusts the angle of attack distribution along the span. This enhances aerodynamic efficiency while delaying blade stall and flow separation.

In structural dynamics, pre-twist induces stiffness coupling between the chordwise and flapwise bending directions via off-diagonal stiffness matrix terms. Concurrently, increased pre-twist angles enhance torsional stiffness, raising the torsional frequencies [1,46]. Fig. 9 illustrates a representative coupled flapwise–chordwise bending mode in Carnegie's 30° pre-twisted rectangular cantilever blade. Example of pre-twist in aeroengine blades are shown in Fig. 10.

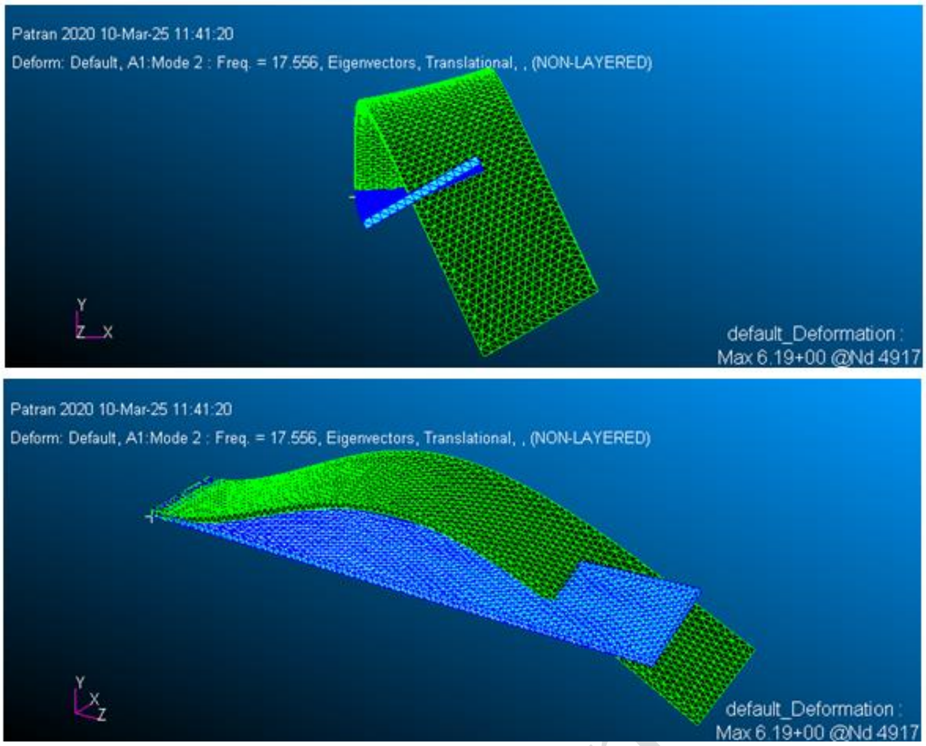

Fig. 9. Coupled flapwise–chordwise bending mode shape of Carnegie's 30° pre-twisted rectangular cantilever blade

Fig. 10. Pre-twist of the Rolls-Royce UltraFan blade [47]

5. Mathematical Modelling Development

For a classical beam of length l, density ρ, and cross-sectional area A, the kinetic energy T and strain energy π in the flapwise bending mode are given by Eqs. (1) and (2), respectively.

$$T = \frac{1}{2}\int_0^l \rho A \dot{y}^2 dz \qquad (1)$$

$$\pi = \frac{1}{2}\int_0^l EI\, {y''}^2 dz \qquad (2)$$

For a shaft model with shear modulus G, torsional constant J, and torsional rigidity C, the kinetic energy and strain energy due to torsion are given by Eqs. (3) and (4).

$$T = \frac{1}{2}\int_0^l \rho J \dot{\theta}^2 dz \qquad (3)$$

$$\pi = \frac{1}{2}\int_0^l GJ\, \theta'^2 dz \qquad (4)$$

The term ρJ represents the mass moment of inertia about the center of gravity ($I_{c.g.}$). When the elastic axis coincides with the centroid (i.e., in the absence of static imbalance), ρJ equals the mass moment of inertia about the elastic axis ($I_{c.f.}$) [1]. Let *n* denote the number of modes, *t* the time, *z* the spanwise coordinate, x the chordwise bending displacement, $T_{b,x}$ the generalized coordinate for chordwise bending, *i* the mode number, and $X^{(i)}$ the i-th chordwise bending mode shape. Using these definitions, Eq. (5) can be expressed.

$$x = \sum_{i=1}^{n} T_{b,x_i} X^{(i)} \qquad (5)$$

Similarly, flapwise bending deflection *y* and torsional deformation *θ* are introduced. The generalized coordinate vector $\vec{T}_{3n\times1}$is expressed by Eq. (6).

$$\vec{T}_{3n\times1} = \begin{Bmatrix} \vec{T}_{b,y_{n\times1}} \\ \vec{T}_{b,x_{n\times1}} \\ \vec{T}_{\theta_{n\times1}} \end{Bmatrix}_{3n\times1} \qquad (6)$$

Let *j* denote an additional mode index, ϕ_{x_j} the j-th chordwise bending trial function, and $c_{b,x_j}^{(i)}$ the Ritz constant (or j-th eigenvector component) corresponding to the i-th mode. With these definitions, Eq. (7) expresses the i-th chordwise bending mode shape, $X^{(i)}$. The corresponding mode shape vector is given by Eq. (8).

$$X^{(i)} = \sum_{j=1}^{n} c_{b,x_j}^{(i)} \phi_{x_j} \qquad (7)$$

$$\vec{X} = \begin{Bmatrix} X^{(1)} \\ \vdots \\ X^{(n)} \end{Bmatrix} = \begin{Bmatrix} c_{b,x_1}^{(1)}\phi_{x_1} + \cdots + c_{b,x_n}^{(1)}\phi_{x_n} \\ \vdots \\ c_{b,x_1}^{(n)}\phi_{x_1} + \cdots + c_{b,x_n}^{(n)}\phi_{x_n} \end{Bmatrix} \qquad (8)$$

Trial functions are categorized into admissible and comparison trial functions. Admissible trial functions, typically simple functions, satisfy only the geometric boundary conditions (e.g., displacement and slope), and therefore require more terms for accurate results. Comparison trial functions satisfy both the geometric and natural (or physical) boundary conditions (e.g., shear force and bending moment), offering greater accuracy with fewer terms. The resulting mode shapes match the number of DOFs and are represented by a modal vector. Square stiffness and mass matrices, with dimensions matching the DOF count, are then assembled. Importantly, the concepts of eigenvectors and mode shapes in the Ritz method differ fundamentally from those in the assumed-modes method [42].

Based on the energy term discretization, the mass and stiffness matrix elements are obtained from Eqs. (9) and (10). Introducing the eigenvalue λ leads to the eigenvalue problem formulated in Eq. (11), and subsequently to the system equation given in Eq. (12) [42].

$$\rightarrow m_{ij} = \int_0^l \rho A \phi_{y_i} \phi_{y_j} dz \qquad (9)$$

$$\rightarrow k_{y_{ij}} = \int_0^l EI \phi''_{b,y_i} \phi''_{b,y_j} dz \qquad (10)$$

$$\rightarrow ([k] - \lambda\, [m])\vec{c} = \vec{0} \qquad (11)$$

$$\rightarrow |[k] - \omega^2 [m]| = \vec{0} \qquad (12)$$

For cantilever beam bending, the geometric boundary conditions enforce zero deflection and zero slope at the fixed root (Eq. (11)). At the free tip, the natural boundary conditions require zero bending moment *M* and zero shear force *V* (Eq. (12)), as these quantities for a continuous beam are expressed by Eqs. (15) and (16).

$$x, y(z = 0, t) = 0\,, x', y'(z = 0, t) = 0 \qquad (13)$$

$$\begin{aligned} V(z = l, t) = 0 &\rightarrow x^{(3)}, y^{(3)}(z = l, t) = 0 \\ M\,(z = l, t) = 0 &\rightarrow x'', y''(z = l, t) = 0 \end{aligned} \qquad (14)$$

$$M\,(z, t) = EIy''(z, t) \qquad (15)$$

$$V(z, t) = EIy^{(3)}(z, t) \qquad (16)$$

For cantilever beams, admissible trial functions, such as Eq. (17), or comparison trial functions, like the beam's bending mode shape [42], may be employed.

$$\phi = \left(\frac{z}{l}\right)^{i+1}, i = 1,2, \dots, n \qquad (17)$$

For a cantilever shaft under torsion, the geometric boundary condition enforces zero rotation θ at the fixed root (Eq. (18)), while the natural boundary condition requires zero torsional moment M_t at the free tip (Eq. (19)). The torsional moment in the shaft is given by Eq. (20).

$$\theta\,(z = 0, t) = 0 \qquad (18)$$

$$M_t\,(z = l, t) = 0 \rightarrow \theta'(z = l, t) = 0 \qquad (19)$$

$$M_t\,(z, t) = GJ\theta'(z, t) \qquad (20)$$

For cantilever shafts, the admissible trial function can be expressed by Eq. (21) or the comparison trial function, such as the shaft's torsion mode shape (Eq. (22)), may be employed**.**

$$\phi = \left(\frac{z}{l}\right)^{i}, i = 1,2, \dots, n \qquad (21)$$

$$\phi = \frac{sin(2i - 1)\,\pi z}{2l}, i = 1,2, \dots, n \qquad (22)$$

The area moments of inertia about the *x*-axis (I_x) and *y*-axis (I_y) are defined by Eqs. (23) and

(24), respectively. The governing equation for flapwise and chordwise bending, as well as torsional vibrations of a cantilevered beam–shaft model, is given by Eq. (25), with the global mass and stiffness matrices specified in Eqs. (26) and (27). The corresponding submatrices are expressed in Eqs. (28)–(33).

$$I_x = \int y^2 dA \qquad (23)$$

$$I_y = \int x^2 dA \qquad (24)$$

$$[M]_{3n\times3n}\ddot{\vec{q}}_{3n\times1} + [K]_{3n\times3n}\vec{q}_{3n\times1} = \vec{F}_{3n\times1} \qquad (25)$$

$$[M] = \begin{bmatrix} [m_y] & [0] & [0] \\ [0] & [m_x] & [0] \\ [0] & [0] & [m_\theta] \end{bmatrix} \qquad (26)$$

$$[K] = \begin{bmatrix} [k_y] & [0] & [0] \\ [0] & [k_x] & [0] \\ [0] & [0] & [k_\theta] \end{bmatrix} \qquad (27)$$

$$[m_y] = \sum_{i=1}^{n}\sum_{j=1}^{n}\int_0^l \rho A \phi_{y_i}\,\phi_{y_j}\,dz \qquad (28)$$

$$[m_x] = \sum_{i=1}^{n}\sum_{j=1}^{n}\int_0^l \rho A \phi_{x_i}\,\phi_{x_j}\,dz \qquad (29)$$

$$[m_\theta] = \sum_{i=1}^{n}\sum_{j=1}^{n}\int_0^l I_{c.f.}\phi_{\theta_i}\,\phi_{\theta_j}\,dz \qquad (30)$$

$$[k_y] = \sum_{i=1}^{n}\sum_{j=1}^{n}\int_0^l EI_x \phi''_{y_i}\,\phi''_{y_j}\,dz \qquad (31)$$

$$[k_x] = \sum_{i=1}^{n}\sum_{j=1}^{n}\int_0^l EI_y \phi''_{x_i}\,\phi''_{x_j}\,dz \qquad (32)$$

$$[k_\theta] = \sum_{i=1}^{n}\sum_{j=1}^{n}\int_0^l C\,\phi'_{\theta_i}\,\phi'_{\theta_j}\,dz \qquad (33)$$

The horizontal and vertical dimensionless offsets between the center of gravity (CG) and the elastic axis (EA) are defined in Eqs. (34) and (35), respectively.

$$x_I = \frac{r_x}{b} \qquad (34)$$

$$y_I = \frac{r_y}{b} \qquad (35)$$

The mass moment of inertia about the center of gravity, $I_{c.g.}$, defined in Eq. (36), is used in the kinetic energy expression in Eq. (37) for cross-sections with static imbalance [1].

$$I_{c.g.} = I_o = \rho I_p = \rho\left(I_x + I_y\right) \qquad (36)$$

$$T = \frac{1}{2}\int_0^l \left[\rho A(\dot{x} + r_y\dot{\theta})^2 + \rho A(\dot{y} + r_x\dot{\theta})^2 + I_{c.g.}\dot{\theta}^2\right] dz \qquad (37)$$

the mass moment of inertia about the elastic axis (shear center or center of flexure), $I_{c.f.}$, defined in Eq. (38), is used in the derived kinetic energy expression in Eq. (39) [1].

$$I_{c.f.} = I_{c.g.} + \rho A(r_y^2 + r_x^2) \qquad (38)$$

$$\rightarrow T = \frac{1}{2}\int_0^l \left[\rho A\left[\dot{x}^2 + {r_y}^2\dot{\theta}^2 + 2\dot{x}r_y\dot{\theta} + \dot{y}^2 + {r_x}^2\dot{\theta}^2 + 2\dot{y}r_x\dot{\theta}\right] + I_{c.g.}\dot{\theta}^2\right] dz$$

$$\rightarrow T = \frac{1}{2}\int_0^l \left[\rho A(\dot{x}^2 + \dot{y}^2) + \dot{\theta}^2\left(I_{c.g.} + \rho A{r_y}^2 + \rho A{r_x}^2\right) + 2\rho A\dot{\theta}\left(\dot{x}r_y + \dot{y}r_x\right)\right] dz$$

$$\rightarrow T = \frac{1}{2}\int_0^l \left[\rho A(\dot{x}^2 + \dot{y}^2) + \dot{\theta}^2 I_{c.f.} + 2\rho A\dot{\theta}\left(\dot{x}r_y + \dot{y}r_x\right)\right] dz \qquad (39)$$

For asymmetric airfoil cross-sections, the kinetic energy discretization under simple harmonic oscillation assumptions (Eq.(40)) yields the modified global mass matrix formulation in Eq. (41), with the corresponding submatrices defined in Eqs. (42)–(45).

$$x = X\,cos(\omega t)\,, y = Y\,cos(\omega t)\,, \theta = \Theta\,cos(\omega t) \qquad (40)$$

$$\rightarrow [M] = \begin{bmatrix} [m_y] & [0] & [m_{y\theta}] \\ [0] & [m_x] & [m_{x\theta}] \\ [m_{\theta y}] & [m_{\theta x}] & [m_\theta] \end{bmatrix} \qquad (41)$$

$$\left[m_{y\theta}\right] = \int_0^l \rho A \phi_{y_i}\,\phi_{\theta j}\,r_x\,dz \qquad (42)$$

$$[m_{x\theta}] = \int_0^l \rho A \phi_{x_i}\phi_{\theta_j} r_y\,dz \qquad (43)$$

$$\left[m_{\theta y}\right] = \int_0^l \rho A \phi_{\theta i}\,\phi_{y_j}\,r_x\,dz \qquad (44)$$

$$[m_{\theta x}] = \int_0^l \rho A \phi_{\theta i}\,\phi_{x j}\,r_y\,dz \qquad (45)$$

Modal analysis of pre-twisted blades requires both a global root-fixed coordinate system and local section-aligned coordinate systems along the span (Fig. 11). Sectional moments of inertia are evaluated separately about the centroid and the shear center (Fig. 12), each within its respective coordinate system [1]. Based on the definitions of the moments of inertia and the local and global coordinate systems, Eqs. ((46)–(51)) hold [41].

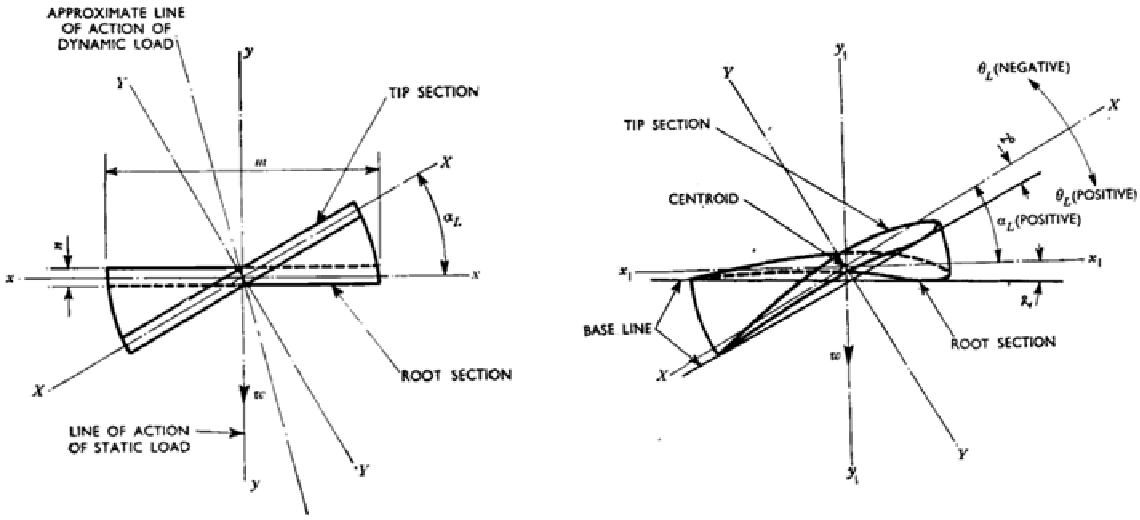

Fig. 11. Global and local coordinate systems about the centroid and shear center for the rectangular (left) and airfoil (right) cross-sections [1]

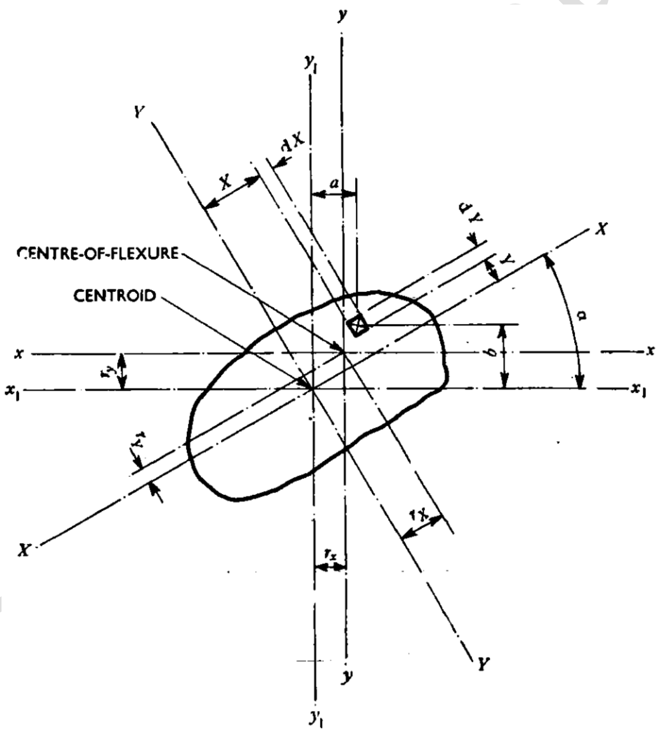

Fig. 12. CG and EA locations and static imbalances in the global and local coordinate systems [1]

$$I_{xx} = I_{YY}\,sin^2\,\alpha + I_{XX}\,cos^2\,\alpha + I_{XY}\,sin\,2\alpha \tag{46}$$

$$\xrightarrow{I_{XY}=0} I_{xx} = I_{YY}\,sin^2\,\alpha + I_{XX}\,cos^2\,\alpha \tag{47}$$

$$I_{XY} = 0 \rightarrow I_{yy} = I_{YY}\, cos^2\, \alpha + I_{XX}\, sin^2\, \alpha \tag{48}$$

$$I_{XY} = 0 \rightarrow I_{xy} = \frac{(I_{YY} - I_{XX})}{2} sin\, 2\alpha \tag{49}$$

$$r_x = r_X cos\alpha - r_Y sin\alpha \tag{50}$$

$$r_y = r_X sin\alpha + r_Y cos\alpha \tag{51}$$

The strain energy for a pretwisted beam is defined in Eq. (52) [1]. Discretization, by governing the maximum strain energy (Eq.(53)), yields the global stiffness matrix of the pretwisted beam–shaft model in Eq. (54), with the corresponding submatrices given in Eqs. (55) and (56).

$$\pi = \frac{1}{2} EI_{yy} x''^2 + EI_{xy} x'' y'' + \frac{1}{2} EI_{xx} y''^2 \tag{52}$$

$$\rightarrow \pi_{max} = \frac{1}{2} \sum_i \sum_j c_i c_j \begin{bmatrix} k_{y_{ij}} & k_{yx_{ij}} \\ k_{xy_{ij}} & k_{xx_{ij}} \end{bmatrix}_{2n\times 2n} \tag{53}$$

$$\rightarrow [K] = \begin{bmatrix} [k_{yy}] & [k_{yx}] & [0] \\ [k_{xy}] & [k_{xx}] & [0] \\ [0] & [0] & [k_\theta] \end{bmatrix} \tag{54}$$

$$[k_{yx}] = \int_0^l EI_{xy} \phi''_{y_i} \phi''_{x_j}\, dz \tag{55}$$

$$[k_{xy}] = \int_0^l EI_{xy} \phi''_{x_i} \phi''_{y_j}\, dz \tag{56}$$

Analytical relations describe the functional dependence of torsional stiffness on the pre-twist angle. In this study, analytical formulas are applied to rectangular sections, while experimental results are used for airfoil sections. Letting *b* and *d* denote the width and thickness, respectively, Eq. (57) quantifies the effect of the pre-twist angle α on the torsional rigidity of rectangular cross-sections [1,46].

$$C = \frac{bd^3 G}{3} \left[1 + \frac{1}{6} \left(\frac{b\alpha}{2l} \right)^2 \left(\frac{b}{d} \right)^2 \right] \tag{57}$$

6. Results and Discussion

The modal analysis of Carnegie's pre-twisted blades with various pre-twist angles was conducted using the Ritz method for both the rectangular and airfoil cross-sections. The airfoil cross-sections were examined in four configurations: without static imbalance, with horizontal static imbalance, with vertical static imbalance, and with combined horizontal and vertical static imbalances. The torsional rigidity of the rectangular cross-section blades was determined analytically, while that of the airfoil cross-sections was obtained by fitting a sixth-degree polynomial to experimental data to achieve full accuracy (Fig. 13).

Validation for the rectangular cross-section case (Table 1) was performed using the finite element method with the commercial software MSC Nastran as the computational solver and Patran for pre-processing (Fig. 14). A mesh sensitivity analysis was conducted to achieve convergence (Table 2). Regarding boundary conditions, the blade root was fully constrained in all six degrees of freedom to simulate a fixed-hub condition. For the modal analysis, the Lanczos method (SOL 103) was employed to extract the natural frequencies and mode shapes. The four airfoil-section cases (Table 3) were validated using results from the advanced finite difference method of Subrahmanyam (Figs. 16–18), whose combined horizontal–vertical static imbalance configuration FDM results was further verified against experimental data (Fig. 19).

Table 1. Carnegie' rectangular cross-section blade parameters and corresponding values [1]

Parameter	**Width** (in)	**Thickness** (in)	**Span** (in)	**Young's modulus** (Mpsi)	**Density** $(\frac{lb}{in^3})$
Value	1	0.068	6	30	0.284

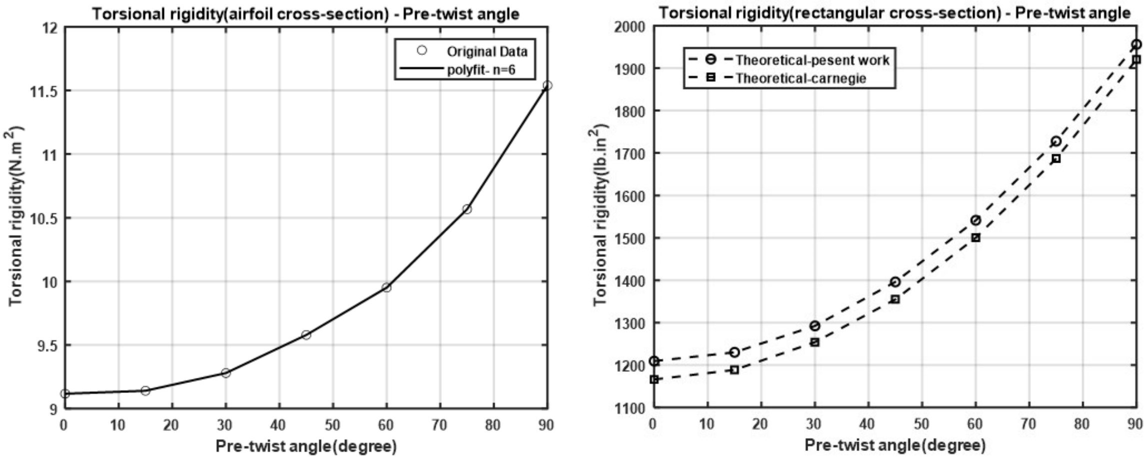

Fig. 13. Torsional rigidity versus pre-twist angle: polynomial fit of experimental data for the airfoil cross-section (left) , and theoretical computation for the rectangular cross-section (right) [1]

Fig. 13 shows that increasing the pre-twist angle increases the blade's torsional rigidity, leading to higher torsional natural frequencies. The slight difference between the present torsional stiffness values for the rectangular cross-section and Carnegie's results arises from the unreported shear modulus in Carnegie's study. In this work, the shear modulus is derived from Poisson's ratio, with a value of 0.3. Table 2 illustrates the convergence of the numerical solution with mesh refinement. Fig. 15 demonstrates that increasing the pre-twist angle in the rectangular cross-section blade raises the torsional frequency, while the coupled flapwise–chordwise bending modes exhibit unpredictable behavior. Their frequencies either decrease, increase, or fluctuate, indicating that prediction without analysis is not feasible. In the case of zero static imbalance, torsional modes remain uncoupled, and only the bending modes are coupled due to pre-twist.

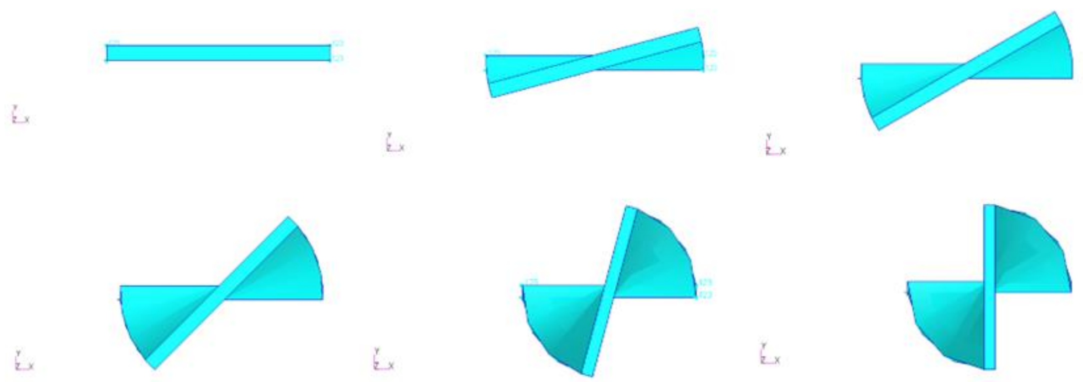

Fig. 14. FE models of Carnegie's rectangular cross-section pre-twisted blades

Table 2. Mesh refinement study (highlighted frequencies indicate torsional modes)

Mode number	Natural freq.(Hz)			
	Global edge length			
	0.24	0.12	0.06	0.03
1	11.705	8.433	3.1696	3.1688
2	49.123	45.969	19.837	19.832
3	71.502	52.794	36.845	36.803
4	198.22	99.704	45.256	45.251
5	231.83	146.76	55.573	55.558
6	274.38	257.85	109.04	109
7	387.31	285.99	112.08	111.95
8	430.74	302.48	180.44	180.38
9	639.94	429.93	191.8	191.57
10	672.84	468.03	254.12	254.1
11	693.59	512.74	269.68	269.56
12	951.92	634.21	278.6	278.25
13	1138.5	689.67	374.63	374.16
14	1144.2	737.36	376.51	376.32
15	1288.3	950.48	429.16	429.14

Table 3. Carnegie's airfoil cross-section blade parameters and the corresponding values [1]

Parameter	**value**	
	Imperial units	**Metric units**
Second moment of area about XX axis (IXX)	0.000084 in^4	34.9633mm^4
Second moment of area about YY axis (IYY)	0.00671 in^4	2792.9mm^4
Span	6 in	0.1524 m
Young's modulus	31 Mpsi	213.73747 Gpa
density	0.284 $\frac{\text{lb}}{\text{in}^3}$	7861.093 $\frac{\text{kg}}{\text{m}^3}$
Cross-sectional area	0.0914 in^2	58.9676 mm^2

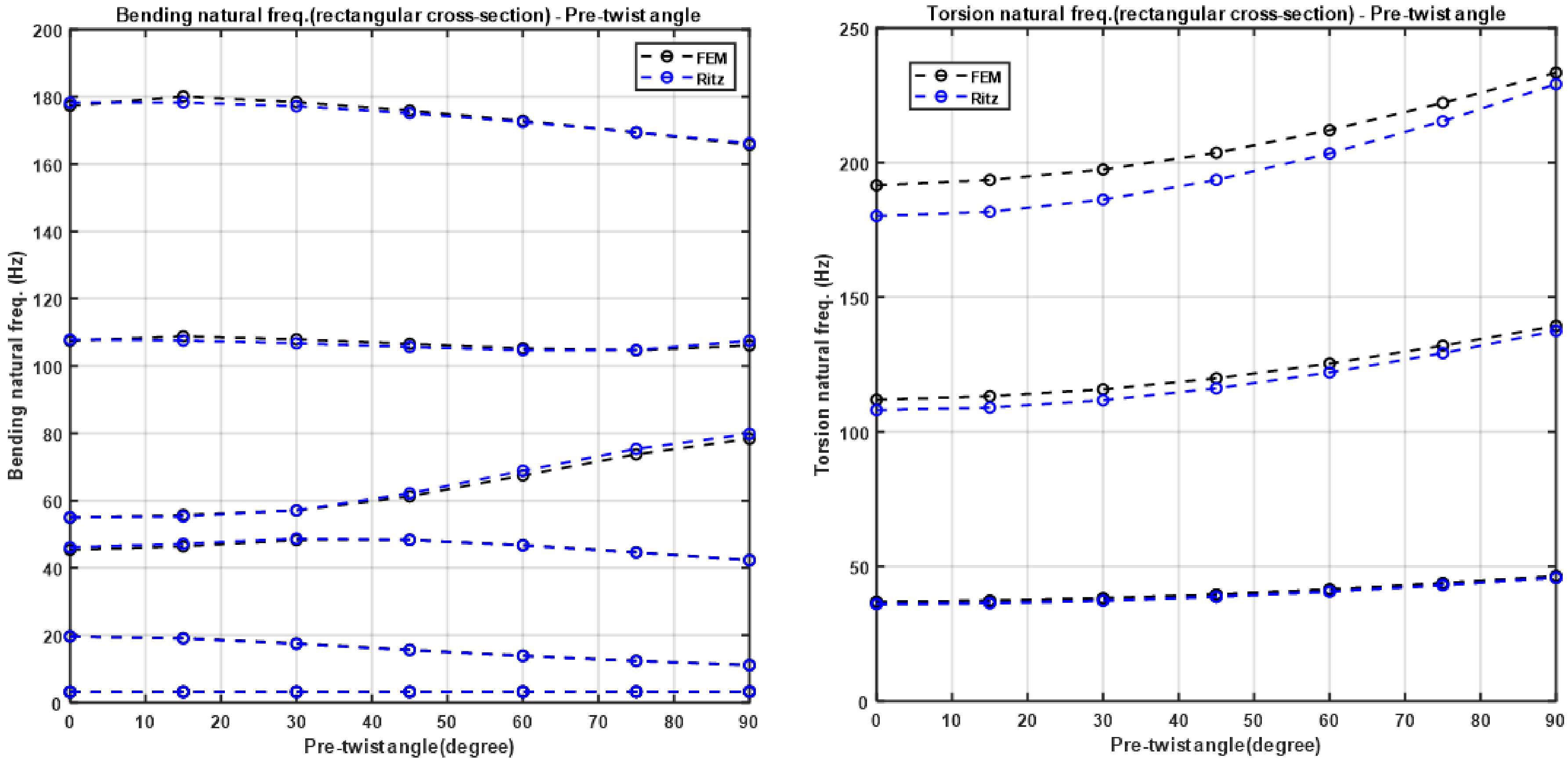

Fig. 15. Coupled flapwise–chordwise bending (left) and Torsional (right) natural frequencies of Carnegie's rectangular cross-section pre-twisted blades, obtained using the FE and Ritz methods

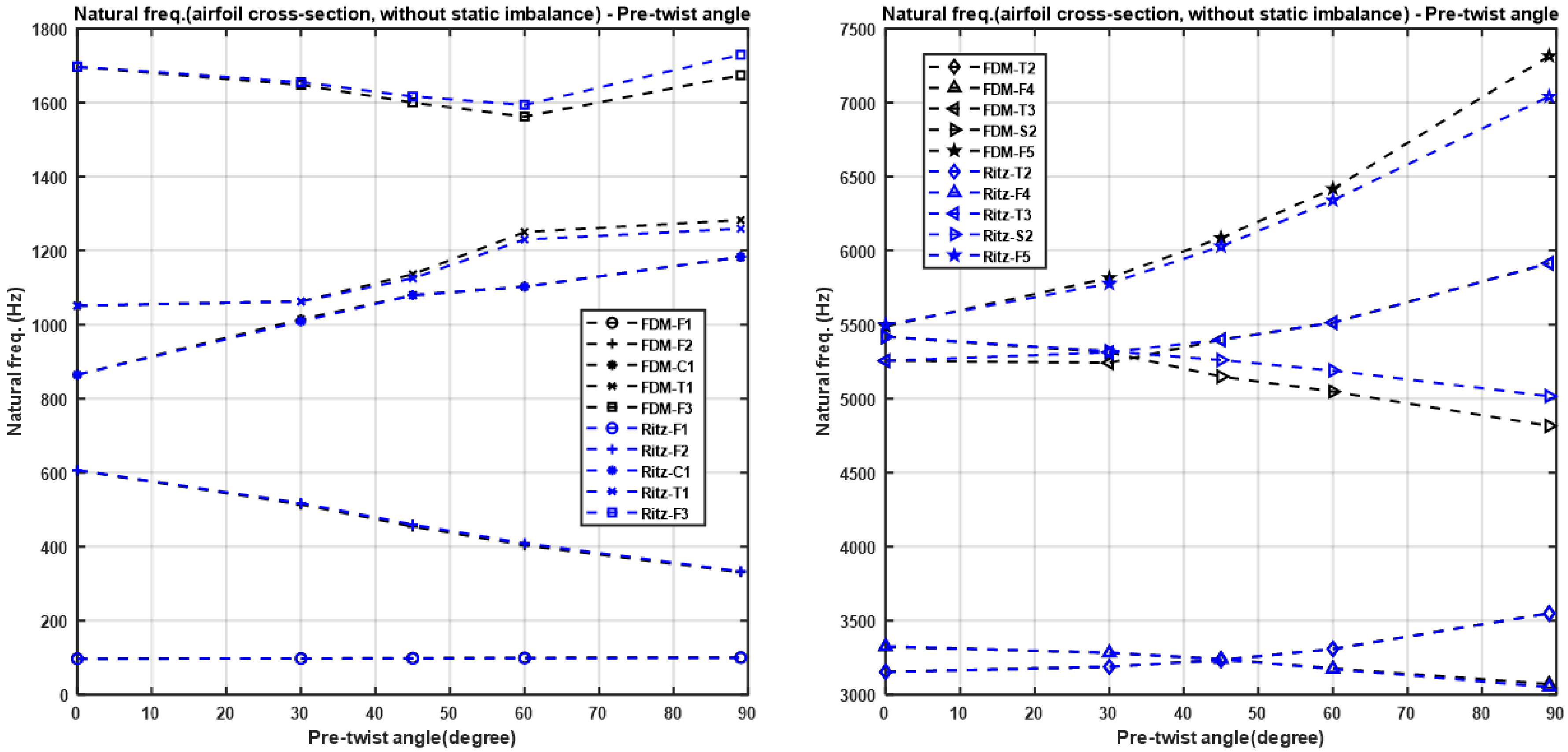

Fig. 16. Torsional and coupled flapwise–chordwise bending natural frequencies of Carnegie's airfoil cross-section pre-twisted blades with zero static imbalances, obtained using the advande FD [2] and Ritz methods

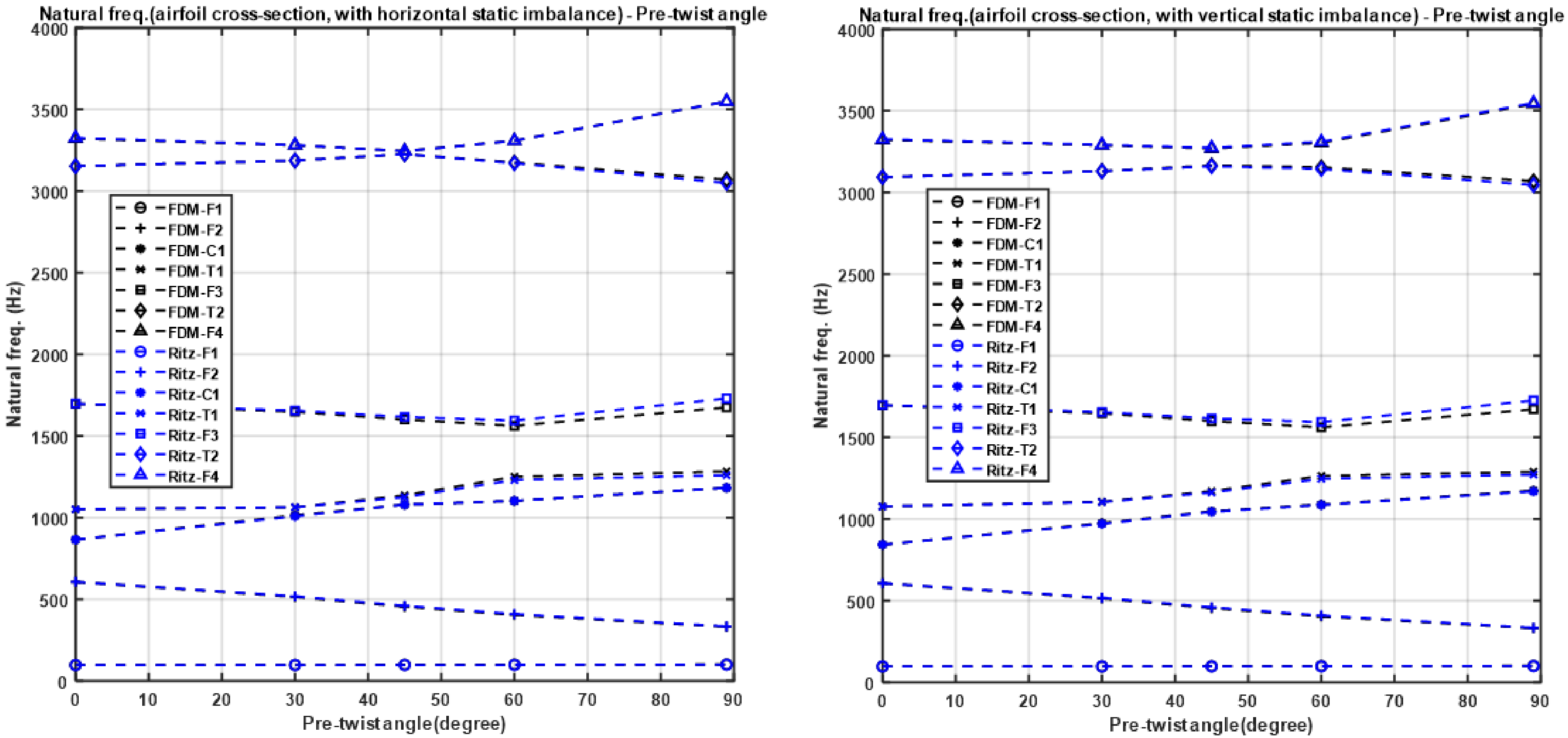

Fig. 17. Coupled flapwise bending–chordwise bending–torsion natural frequencies of Carnegie's airfoil cross-section pre-twisted blades with horizontal (left) and vertical (right) static imbalances, obtained using the advance FD [2] and Ritz methods

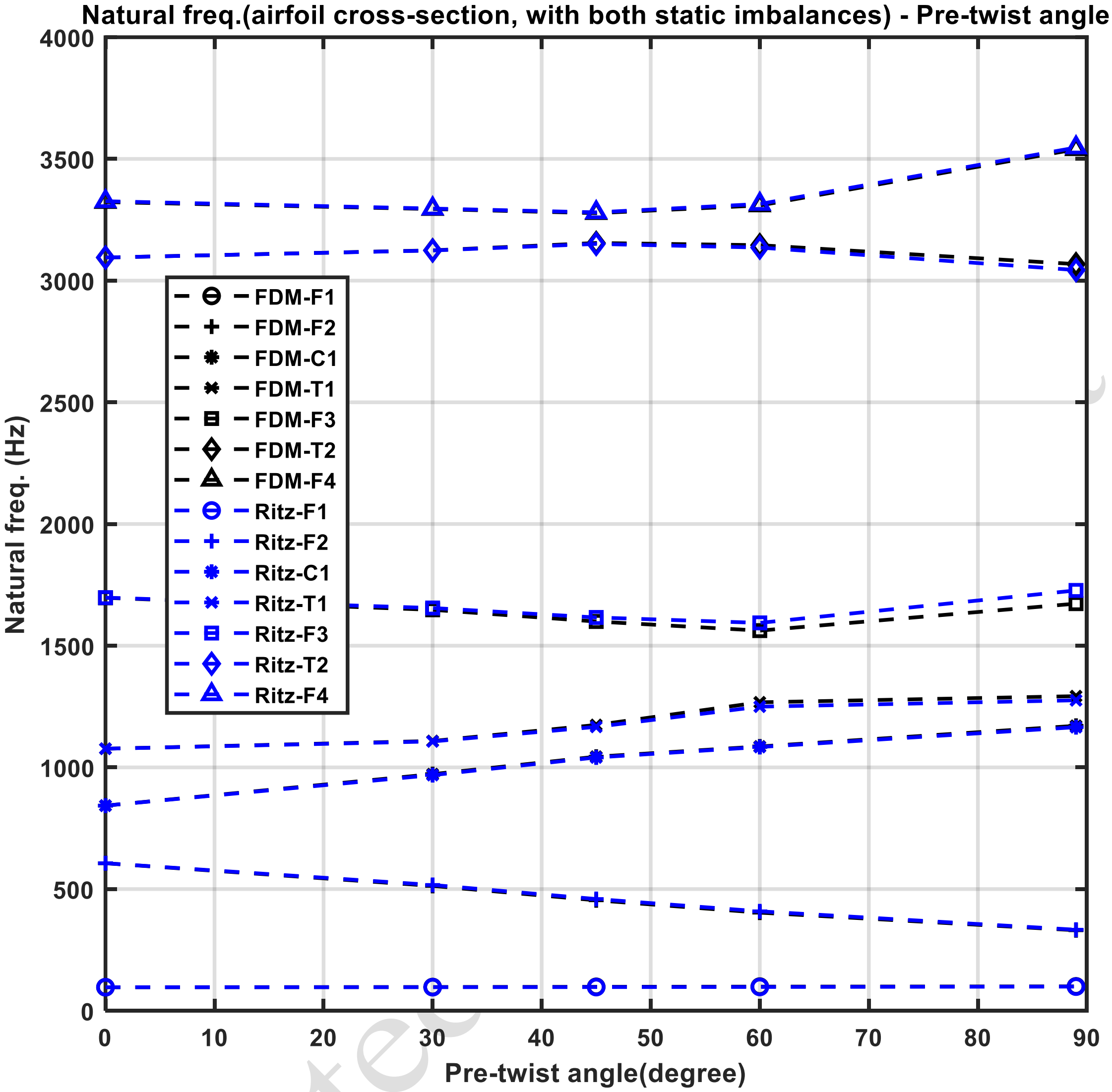

Fig. 18. Coupled flapwise bending–chordwise bending–torsion natural frequencies of Carnegie's airfoil cross-section pre-twisted blades with both horizontal and vertical static imbalances, obtained using the advande FD [2] and Ritz methods

Fig. 16 shows that the modal behavior of the doubly symmetric airfoil-section specimen resembles that of the rectangular cross-section blade, aside from the different rate of torsional stiffness increase with pre-twist angle (Fig. 13). The branches are labeled F, C, and T to indicate that they are initially dominated by flapwise bending, chordwise bending, and torsion, respectively. In contrast, Figs. 17–19 and table 4 show different behavior. For the airfoil-section specimens with static imbalance, increasing the pre-twist angle alters the torsional contribution in the coupled modes due to torsion–bending coupling. As the branches converge, the dominant mode gradually shifts; a branch that is initially torsion-dominated transitions to bending dominance as the branches approach, and is then tracked along the decreasing-frequency branch.

Table 4. A comparison of the Ritz and the Advance FDM [2] natural frequencies in the case 4, the asymmetric airfoil cross-section pre-twisted blade

Modes	Natural frequencies r_x=0.193mm, r_y=1.1938mm					
	Method	pre-twist angle				
		0	30	45	60	89
F1	Ritz	96.7385	97.0441	97.4227	97.9483	99.3631
	FDM	96.737	97.557	98.413	99.313	100.246
	Error %	0.002	-0.526	-1.006	-1.374	-0.881
F2	Ritz	606.235	516.98	459.174	408.674	333.025
	FDM	606.141	513.162	453.978	403.259	330.896
	Error %	0.016	0.744	1.145	1.343	0.643
S1	Ritz	842.904	968.378	1040.81	1083.76	1165.26
	FDM	842.895	972.178	1043.971	1085.937	1170.91
	Error %	0.001	-0.391	-0.303	-0.200	-0.483
T1	Ritz	1076.71	1106.65	1166.54	1249.56	1275.69
	FDM	1076.709	1108.465	1174.357	1267.441	1292.688
	Error %	0.0001	-0.1637	-0.6656	-1.4108	-1.3149
F3	Ritz	1697.43	1654.87	1616.03	1593.74	1727.11
	FDM	1696.647	1647.424	1599.445	1562.017	1672.784
	Error %	0.0461	0.4520	1.0369	2.0309	3.2476
T2	Ritz	3094.95	3123.82	3150.75	3135.84	3043.41
	FDM	3094.922	3124.353	3154.608	3145.672	3067.755
	Error %	0.001	-0.017	-0.122	-0.313	-0.794
F4	Ritz	3326.17	3296.07	3280.49	3314.84	3546.77
	FDM	3322.705	3294.018	3277.243	3308.751	3539.662
	Error %	0.104	0.062	0.099	0.184	0.201

7. Conclusions

This study performed vibration analysis of pre-twisted rectangular and airfoil-section blades using a Ritz-based continuous classical beam–shaft ROM. It was observed that the Ritz method achieves accuracy and precision comparable to experimental, numerical, and finite difference methods in considering pre-twist and horizontal or vertical static imbalance effects.The results indicate that increasing the pre-twist angle raises the natural torsional frequencies and enhances coupling between chordwise and flapwise bending modes. As a result, under static imbalance, varying the pre-twist angle introduces bending–torsion coupling, leading to distinct frequency changes across all branches and causing the initially torsion-dominated branch to either increase or decrease in frequency rather than consistently rise. These non-intuitive behaviors provide valuable insights for structural dynamic assessments and aeroelastic evaluations of blade systems. The proposed framework provides a basis for ROM-based tools capable of performing computationally efficient aeroelastic analyses of continuous blade models, blade rows, and integrated gas turbines.

Appendix A: **Derivation of the Global Mass Matrix**

In this section, the detailed steps for deriving the global mass matrix, as referenced in Section 5, are presented.

$$T=\frac{1}{2}\int_0^l\Big\{\Big[\rho A(X^2\,\omega^2\,sin^2(\omega t)+Y^2\,\omega^2\,sin^2(\omega t))+\Theta^2\,\omega^2\,sin^2(\omega t)\,I_{c.f.}$$
$$+2\rho A(-\Theta\,\omega\,sin(\omega t))\Big((-X\,\omega\,sin(\omega t))r_y+(-Y\omega\,sin(\omega t))r_x\Big)\Big]\Big\}\,dz$$
$$=\frac{1}{2}\int_0^l\{[\rho A\omega^2\,sin^2(\omega t)\,(X^2\ +Y^2\,)+\Theta^2\,\omega^2\,sin^2(\omega t)\,I_{c.f.}$$
$$+2\rho A\Theta\,\omega^2\,sin^2(\omega t)\,(X\,r_y+Yr_x)]\}dz$$

$$\rightarrow\ T_{max}=\frac{1}{2}\int_0^l\{[\rho A\omega^2(X^2\ +Y^2\,)+\Theta^2\,\omega^2 I_{c.f.}+2\rho A\Theta\,\omega^2(X\,r_y+Yr_x)]\}dz$$

$$=\frac{1}{2}\int_0^l\{[\rho A\omega^2(X^2\ +Y^2\,)+\Theta^2\,\omega^2 I_{c.f.}+2\rho A\omega^2(\Theta X\,r_y+\Theta Y r_x)]\}dz$$

$$\rightarrow\ T^*{}_{max}=\frac{1}{2}\int_0^l\{[\rho A(X^2\ +Y^2\,)+\Theta^2\,I_{c.f.}+2\rho A(\Theta X\,r_y+\Theta Y r_x)]\}dz$$

$$=\frac{1}{2}\int_0^l\{[\rho A(X^2\ +Y^2\,)+\Theta^2\,I_{c.f.}+\rho A(\Theta X\,r_y+\Theta Y r_x)+\rho A(\Theta X\,r_y+\Theta Y r_x)]\}dz$$

$$=\frac{1}{2}\int_0^l\left\{\left[\rho A\left(\sum_{i=1}^{n}X_i\sum_{j=1}^{n}X_j+\sum_{i=n}^{2n}Y_i\sum_{j=n}^{2n}Y_j\right)+\sum_{i=2n}^{3n}\Theta_i\sum_{j=2n}^{3n}\Theta_j\ I_{c.f.}\right.\right.$$
$$+\rho A\left(\sum_{i=2n}^{3n}\Theta_i\sum_{j=1}^{n}X_j\ r_y+\sum_{i=2n}^{3n}\Theta_i\sum_{j=n}^{2n}Y_j\ r_x+\sum_{j=2n}^{3n}\Theta_j\sum_{i=1}^{n}X_i\,r_y\right.$$
$$\left.\left.\left.+\sum_{j=2n}^{3n}\Theta_j\sum_{i=n}^{2n}Y_i\ r_x\right)\right]\right\}dz$$

$$T^*{}_{max}=\frac{1}{2}\int_0^l\left\{\left[\rho A\left(\sum_{i=1}^{n}c_i\phi_{x_i}\sum_{j=1}^{n}c_j\phi_{x_j}+\sum_{i=n}^{2n}c_i\phi_{y_i}\sum_{j=n}^{2n}c_j\phi_{y_j}\right)\right.\right.$$
$$+\sum_{i=2n}^{3n}c_i\phi_{\theta_i}\sum_{j=2n}^{3n}c_j\phi_{\theta_j}\ I_{c.f.}$$
$$+\rho A\left(\sum_{i=2n}^{3n}c_i\phi_{\theta_i}\sum_{j=1}^{n}c_j\phi_{x_j}\ r_y+\sum_{i=2n}^{3n}c_i\phi_{\theta_i}\sum_{j=n}^{2n}c_j\phi_{y_j}\ r_x\right.$$
$$\left.\left.\left.+\sum_{j=2n}^{3n}c_j\phi_{\theta_j}\sum_{i=1}^{n}c_i\phi_{x_i}\ r_y+\sum_{j=2n}^{3n}c_j\phi_{\theta_j}\sum_{i=n}^{2n}c_i\phi_{y_i}\ r_x\right)\right]\right\}dz$$

$$= \frac{1}{2}\sum \sum c_i\, c_j \int_0^l \Big\{\Big[\rho A\left(\phi_{x_i}\phi_{x_j} + \phi_{y_i}\phi_{y_j}\right) + \phi_{\theta_i}\phi_{\theta_j} I_{c.f.}$$
$$+ \rho A\left(\phi_{\theta_i}\phi_{x_j} r_y + \phi_{\theta_i}\phi_{y_j} r_x + \phi_{\theta_j}\phi_{x_i} r_y + \phi_{\theta_j}\phi_{y_i} r_x\right)\Big]\Big\} dz$$

Appendix B: **Derivation of the Global Stiffness Matrix**

In this section, the detailed steps for deriving the global Stiffness matrix, as referenced in Section 5, are presented.

$$\pi = \frac{cos^2(\omega t)}{2}\left[\int_0^l EI_{yy}Y''^2 dz + 2\int_0^l EI_{xy}Y'' X'' dz + \int_0^l EI_{xx}X''^2 dz\right]$$

$$\rightarrow\ \pi_{max} = \frac{1}{2}\left[\int_0^l EI_{yy}Y''^2 dz + 2\int_0^l EI_{xy}Y'' X'' dz + \int_0^l EI_{xx}X''^2 dz\right]$$

$$\rightarrow \pi_{max} = \frac{1}{2}\left[\int_0^l EI_{yy}\sum_{i=1}^{n} Y_i'' \sum_{j=1}^{n} Y_j''\ dz + \int_0^l EI_{xy}\sum_{i=1}^{n} Y_i'' \sum_{j=n}^{2n} X_j''\ dz + \int_0^l EI_{xy}\sum_{i=n}^{2n} X_i'' \sum_{j=1}^{n} Y_j''\ dz + \int_0^l EI_{xx}\sum_{i=n}^{2n} X_i'' \sum_{j=n}^{2n} Y_j''\ dz\right]$$

$$= \frac{1}{2}\left[\int_0^l EI_{yy}\sum_{i=1}^{n} c_{y_i}\phi''_{y_i} \sum_{j=1}^{n} c_{y_j}\phi''_{y_j}\ dz + \int_0^l EI_{xy}\sum_{i=1}^{n} c_{y_i}\phi''_{y_i} \sum_{j=n}^{2n} c_{x_j}\phi''_{x_j}\ dz + \int_0^l EI_{xy}\sum_{i=n}^{2n} c_{x_i}\phi''_{x_i} \sum_{j=1}^{n} c_{y_j}\phi''_{y_j}\ dz + \int_0^l EI_{xx}\sum_{i=n}^{2n} c_{x_i}\phi''_{x_i} \sum_{j=n}^{2n} c_{x_j}\phi''_{x_j}\ dz\right]$$

$$= \frac{1}{2}\left[\sum_{i=1}^{n}\sum_{j=1}^{n} c_{y_i}c_{y_j}\int_0^l EI_{yy}\phi''_{y_i}\,\phi''_{y_j}\, dz + \sum_{i=1}^{n}\sum_{j=n}^{2n} c_{y_i}c_{x_j}\int_0^l EI_{xy}\phi''_{y_i}\,\phi''_{x_j}\, dz + \sum_{i=n}^{2n}\sum_{j=1}^{n} c_{x_i}c_{y_j}\int_0^l EI_{xy}\phi''_{x_i}\,\phi''_{y_j}\, dz + \sum_{i=n}^{2n}\sum_{j=n}^{2n} c_{x_i}c_{x_j}\int_0^l EI_{xx}\phi''_{x_i}\,\phi''_{x_j}\, dz\right]$$

$$= \frac{1}{2}\left[\sum_{i=1}^{n}\sum_{j=1}^{n} c_{y_i}c_{y_j}\, k_{y_{ij}} + \sum_{i=1}^{n}\sum_{j=n}^{2n} c_{y_i}c_{x_j}k_{yx_{ij}} + \sum_{i=n}^{2n}\sum_{j=1}^{n} c_{x_i}c_{y_j}\, k_{xy_{ij}} + \sum_{i=n}^{2n}\sum_{j=1}^{n} c_{x_i}c_{y_j}\, k_{xx_{ij}}\right]$$

References

[1] Carnegie, W., "Vibrations of Pre-Twisted Cantilever Blading," *Proceedings of the*

Institution of Mechanical Engineers, Vol. 173, No. 1, 1959, pp. 343–374. https://doi.org/10.1243/PIME_PROC_1959_173_038_02

[2] Subrahmanyam, K. B., and Kaza, K. R. V., "Improved Methods of Vibration Analysis of Pretwisted, Airfoil Blades," presented at the XVIth International Congress of Theoretical and Applied Mechanics, Lyngby, 1984.

[3] Carnegie, W., and Dawson, B., "Vibration Characteristics of Pre-Twisted Blades of Asymmetrical Aerofoil Cross-Section," *Aeronautical Quarterly, Cambridge University Press*, Vol. 22, No. 3, 1971, pp. 257–273. https://doi.org/10.1017/S0001925900005813

[4] DiPrima, R. C., and Handelman, G. H., "Vibrations of Twisted Beams," *Quarterly of Applied Mathematics*, Vol. 12, No. 3, 1954, pp. 241–259. https://doi.org/10.1090/qam/64619

[5] Carnegie, W., "Vibrations of Pretwisted Cantilver Blading: An Additional Effect Due to Torsion," *Proceedings of the Institution of Mechanical Engineers*, 1962.

[6] Carnegie, W., "Vibrations of Pre-Twisted Cantilever Blading Allowing for Rotary Inertia and Shear Deflection," *Journal of Mechanical Engineering Science*, Vol. 6, No. 2, 1963, pp. 105–109. https://doi.org/10.1243/jmes_jour_1964_006_019_02

[7] Carnegie, W., "A Note on the Application of the Variational Method to Derive the Equations of Dynamic Motion of a Pretwisted Cantilever Blade Mounted on the Periphery of a Rotating Disc Allowing for Shear Deflection, Rotary Inertia and Torsion Bending," *Bull. Mech. Engng Education 5, 221*, 1966.

[8] Houbolt, J. C., and Brooks, G. W., "Differential Equations of Motion for Combined Flapwise Bending, Chordwise Bending, and Torsion of Twisted Nonuniform Rotor Blades," January 1958.

[9] Dawson, B., "Coupled Bending-Bending Vibrations of Pre-Twisted Cantilever Blading Treated by the Rayleigh-Ritz Energy Method," *Journal of Mechanical Engineering Science*, Vol. 10, No. 5, 1968, pp. 381–388. https://doi.org/10.1243/JMES_JOUR_1968_010_060_02

[10] Zhu, T., "The Vibrations of Pre-Twisted Rotating Timoshenko Beams by the Rayleigh–Ritz Method," *ResearchGate*, 2010. https://doi.org/10.1007/s00466-010-0550-9

[11] Yao, M., Wang, S., Niu, Y., Wu, Q., and Wang, C., "Vibration Characteristics of Pre-Twisted Rotating Ti-SiC Composite Airfoil Blade," *Applied Mathematical Modelling*, Vol. 128, 2024, pp. 392–409. https://doi.org/10.1016/j.apm.2024.01.033

[12] Oh, Y., and Yoo, H. H., "Vibration Analysis of a Rotating Pre-Twisted Blade Considering the Coupling Effects of Stretching, Bending, and Torsion," *Journal of Sound and Vibration*, Vol. 431, 2018, pp. 20–39. https://doi.org/10.1016/j.jsv.2018.05.030

[13] Rao, J. S., and Carnegie, W., "Solution of the Equations of Motion of Coupled-Bending Bending Torsion Vibrations of Turbine Blades by the Method of Ritz-Galerkin," *International Journal of Mechanical Sciences*, Vol. 12, No. 10, 1970, pp. 875–882. https://doi.org/10.1016/0020-7403(70)90024-X

[14] Rao, J. S., "Flexural Vibration of Pretwisted Tapered Cantilever Blades," *Journal of Engineering for Industry*, Vol. 94, No. 1, 1972, pp. 343–346. https://doi.org/10.1115/1.3428148

[15] Rao, J. S., "Coupled Bending Bending Torsion Vibrations of Cantilever Beams," *Journal of the Aeronautical Society of India 24(1), 265–268*, 1972.

[16] Subrahmanyam, K. B., Kulkarni, S. V., and Rao, J. S., "Coupled Bending-Bending Vibrations of Pre-Twisted Cantilever Blading Allowing for Shear Deflection and Rotary Inertia by the Reissner Method," *International Journal of Mechanical Sciences*, Vol. 23, No. 9, 1981, pp. 517–530. https://doi.org/10.1016/0020-7403(81)90058-8

[17] Subrahmanyam, K. B., Kulkarni, S. V., and Rao, J. S., "Application of the Reissner Method to Derive the Coupled Bending-Torsion Equations of Dynamic Motion of

Rotating Pretwisted Cantilever Blading with Allowance for Shear Deflection, Rotary Inertia, Warping and Thermal Effects," *Journal of Sound and Vibration*, Vol. 84, No. 2, 1982, pp. 223–240. https://doi.org/10.1016/S0022-460X(82)80005-9

[18] Martin, A. I., "Approximation for the Effect of Twist on the Vibration of a Turbine Blade," *Aeronautical Quarterly*, Vol. 8, No. 3, 1957, pp. 291–308. https://doi.org/10.1017/S0001925900010581

[19] Baxy, A., and Sarkar, A., "Natural Frequencies of Rotating Twisted Beams: A Perturbation Method Based Approach," *Meccanica*, Vol. 55, No. 10, 2020, pp. 2075–2089. https://doi.org/10.1007/s11012-020-01238-7

[20] Carnegie, W., Dawson, B., and Thomas, J., "Vibration Characteristics of Cantilever Blading," *Proceedings of the Institution of Mechanical Engineers, Conference Proceedings*, Vol. 180, No. 9, 1965, pp. 71–89. https://doi.org/10.1243/PIME_CONF_1965_180_235_02

[21] Montoya, J., "Coupled Bending and Torsional Vibrations in a Twisted Rotating Blade," *Brown-Boveri Review, Vol. 53, No. 3*, 1966.

[22] Dawson, B., and Carnegie, W., "Modal Curves of Pre-Twisted Beams of Rectangular Cross-Section," *Journal of Mechanical Engineering Science*, Vol. 11, No. 1, 1969, pp. 1–13. https://doi.org/10.1243/JMES_JOUR_1969_011_003_02

[23] Carnegie, W., and Thomas, J., "The Coupled Bending—Bending Vibration of Pre-Twisted Tapered Blading," *Journal of Engineering for Industry*, Vol. 94, No. 1, 1972, pp. 255–266. https://doi.org/10.1115/1.3428120

[24] Mendelson, A., and Gendler, S., "Analytical and Experimental Investigation of Effect of Twist on Vibrations of Cantilever Beams," Mar 01 1951.

[25] Mendelson, A., and Gendler, S., "Analytical Determination of Coupled Bending-Torsion Vibrations of Cantilever Beams by Means of Station Functions - NASA Technical Reports Server (NTRS)," 1951.

[26] Fu, C. C., "Computer Analysis of a Rotating Axial-turbomachine Blade in Coupled Bending-bending-torsion Vibrations," *International Journal for Numerical Methods in Engineering*, Vol. 8, No. 3, 1974, pp. 569–588. https://doi.org/10.1002/nme.1620080312

[27] Rosard, D. D., "Natural Frequencies of Twisted Cantilever Beams," *Journal of Applied Mechanics*, Vol. 20, No. 2, 1953, pp. 241–244. https://doi.org/10.1115/1.4010656

[28] Jarrett, G. W., and Warner, P. C., "The Vibration of Rotating, Tapered-Twisted Beams," *Journal of Applied Mechanics*, Vol. 20, No. 3, 1953, pp. 381–389. https://doi.org/10.1115/1.4010708

[29] Isakson, G., and Eisely, J. G., "Natural Frequencies in Coupled Bending and Torsion of Twisted Rotating and Nonrotating Blades," NASA Contractor Report, National Aeronautics and Space Administration, University Of Michigan, Washington, D. C., 1964.

[30] Slyper, H. A., "Coupled Bending Vibrations of Pretwisted Cantilever Beams," *Journal of Mechanical Engineering Science*, Vol. 4, No. 4, 1962, pp. 365–379. https://doi.org/10.1243/JMES_JOUR_1962_004_050_02

[31] Adair, D., and Jaeger, M., "Vibration Analysis of a Uniform Pre-Twisted Rotating Euler–Bernoulli Beam Using the Modified Adomian Decomposition Method," *Mathematics and Mechanics of Solids*, Vol. 23, No. 9, 2017, pp. 1345–1363. https://doi.org/10.1177/1081286517720843

[32] Gupta, R. S., and Rao, S. S., "Finite Element Eigenvalue Analysis of Tapered and Twisted Timoshenko Beams," *Journal of Sound and Vibration*, Vol. 56, No. 2, 1978, pp. 187–200. https://doi.org/10.1016/S0022-460X(78)80014-5

[33] Sabuncu, M., "Coupled Vibration Analysis of Blades with Angular Pretwist of Cubic Distribution," *AIAA Journal*, Vol. 23, No. 9, 1985, pp. 1424–1430.

https://doi.org/10.2514/3.9102
[34] Sabuncu, M., and Thomas, J., “Vibration Characteristics of Pretwisted Aerofoil Cross-Section Bladepackets under Rotating Conditions,” *AIAA Journal*, Vol. 30, No. 1, 1992, pp. 241–250. https://doi.org/10.2514/3.10905
[35] Yardimoglu, B., and Inman, D., “Coupled Bending-Bending-Torsion Vibration of a Pre-Twisted Beam with Aerofoil Cross-Section by the Finite Element Method,” *Journal of Shock and Vibration*, 2003. https://doi.org/10.1155/2003/354074
[36] Yardimoglu, B., and Yildirim, T., “Finite Element Model for Vibration Analysis of Pre-Twisted Timoshenko Beam,” *Journal of Sound and Vibration*, Vol. 273, Nos. 4–5, 2004, pp. 741–754. https://doi.org/10.1016/j.jsv.2003.05.003
[37] Shukur, Z. M., Neamah, R. A., Abdulsamad, H. J., Al-Ansari, L. S., and Wittayapiyanon, S., “Calculating the Natural Frequency of Pre-Twisted Beam,” *Journal of Engineering and Sustainable Development*, Vol. 28, No. 1, 2024, pp. 1–16. https://doi.org/10.31272/jeasd.28.1.1
[38] Kishore, M. L. P., and Behera, R. K., “Effect of Pretwist on Free Vibration Characteristics Determination of Metallic Curved Blade Replaced with Composite Material,” *Journal of Ocean Research*, Vol. 2, No. 1, 2014, pp. 11–16. https://doi.org/10.12691/jor-2-1-3
[39] Casoni, M., and Benini, E., “A Review of Computational Methods and Reduced Order Models for Flutter Prediction in Turbomachinery,” *Aerospace*, Vol. 8, No. 9, 2021, p. 242. https://doi.org/10.3390/aerospace8090242
[40] Norouzi, A., Shokrollahi, S., and Shafaghat, S., “Classical Flutter Analysis of a Gas Turbine Blade-Row via Ritz-Based ROM (in Persian),” presented at the 15’th International Conference on acoustics and vibration, K. N. Toosi University of Technology, Tehran, Iran, 2025.
[41] Carnegie, W., “Static Bending of Pre-Twisted Cantilever Blading,” *Proceedings of the Institution of Mechanical Engineers*, 1957. https://doi.org/10.1243/PIME_PROC_1957_171_071_02
[42] Rao, S. S., “Vibration of Continuous Systems,” John Wiley & Sons Ltd, Hoboken, NJ, USA, 2019.
[43] Ghalandari, M., Ziamolki, A., Mosavi, A., Shamshirband, S., Chau, K.-W., and Bornassi, S., “Aeromechanical Optimization of First Row Compressor Test Stand Blades Using a Hybrid Machine Learning Model of Genetic Algorithm, Artificial Neural Networks and Design of Experiments,” *Engineering Applications of Computational Fluid Mechanics*, 2019. Retrieved 4 January 2025. https://www.tandfonline.com/doi/abs/10.1080/19942060.2019.1649196
[44] Wang, Y., Xu, S., Zhou, Y., and Zhou, C., “Intercoupling Aeroelastic Stability Topology Optimization for the Design of Bend-twisted Hollow Blade in a Turbomachinery Cascade,” 2023.
[45] Kaza, K., and Kielb, R., “Effects of Mistuning on Bending-Torsion Flutter and Response of a Cascade in Incompressible Flow,” presented at the Dynamics Specialists Conference, Atlanta,GA,U.S.A., 1981. https://doi.org/10.2514/6.1981-602
[46] Rao, J. S., “Turbomachine Blade Vibration,” New Age International publishers, India, 1991.
[47] “Rolls-Royce, LinkedIn,” Aug 22 2024. Retrieved 24 July 2025. https://www.linkedin.com/company/rolls-royce